Surface modulation of silicon nitride ceramics for orthopaedic applications

Ryan M. Bock [a,*], Bryan J. McEntire [a], B. Sonny Bal [a,b], Mohamed N. Rahaman [c], Marco Boffelli [d], Giuseppe Pezzotti [d]

[a] Amedica Corporation, 1885 West 2100 South, Salt Lake City, UT 84119, USA
[b] Department of Orthopaedic Surgery, University of Missouri, Columbia, MO 65212, USA
[c] Department of Materials Science and Engineering, Missouri University of Science and Technology, Rolla, MO 65409, USA
[d] Ceramic Physics Laboratory, Kyoto Institute of Technology, Sakyo-ku, Matsugasaki, 606-8126 Kyoto, Japan

ABSTRACT

Silicon nitride (Si_3N_4) has a distinctive combination of material properties such as high strength and fracture toughness, inherent phase stability, scratch resistance, low wear, biocompatibility, hydrophilic behavior, excellent radiographic imaging and resistance to bacterial adhesion, all of which make it an attractive choice for orthopaedic implants. Unlike oxide ceramics, the surface chemistry and topography of Si_3N_4 can be engineered to address potential *in vivo* needs. Morphologically, it can be manufactured to have an ultra-smooth or highly fibrous surface structure. Its chemistry can be varied from that of a silica-like surface to one which is predominately comprised of silicon-amines. In the present study, a Si_3N_4 bioceramic was subjected to thermal, chemical, and mechanical treatments in order to induce changes in surface composition and features. The treatments included grinding and polishing, etching in aqueous hydrofluoric acid, and heating in nitrogen or air. The treated surfaces were characterized using a variety of microscopy techniques to assess morphology. Surface chemistry and phase composition were determined using X-ray photoelectron and Raman spectroscopy, respectively. Streaming potential measurements evaluated surface charging, and sessile water drop techniques assessed wetting behavior. These treatments yielded significant differences in surface properties with isoelectric points ranging from 2 to 5.6, and moderate to extremely hydrophilic water contact angles from ∼65° to ∼8°. This work provides a basis for future *in vitro* and *in vivo* studies which will examine the effects of these treatments on important orthopaedic properties such as friction, wear, protein adsorption, bacteriostasis and osseointegration.

Statement of Significance

Silicon nitride (Si_3N_4) exhibits a unique combination of bulk mechanical and surface chemical properties that make it an ideal biomaterial for orthopaedic implants. It is already being used for interbody spinal fusion cages and is being developed for total joint arthroplasty. Its surface texture and chemistry are both highly tunable, yielding physicochemical combinations that may lead to enhanced osseointegration and bacterial resistance without compromising bulk mechanical properties. This study demonstrates the ease with which significant changes to Si_3N_4's surface phase composition, charging, and wetting behavior can be induced, and represents an initial step towards a mechanistic understanding of the interaction between implant surfaces and the biologic environment.

© 2015 Acta Materialia Inc. Published by Elsevier Ltd. All rights reserved.

1. Introduction

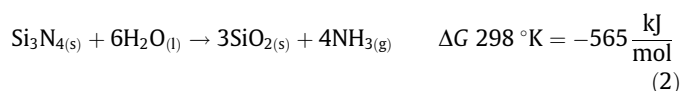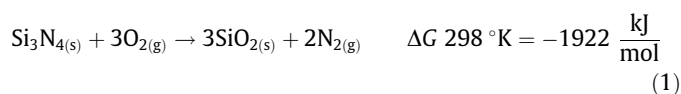Silicon nitride (Si_3N_4) is a non-oxide ceramic that exhibits several unique properties making it attractive for various orthopaedic applications [1–5]. It can be produced with a fully dense microstructure, composed of fibrous interlocking grains, a material referred to as being *in situ* toughened, which exhibits an optimal combination of wear resistance, flexural strength and fracture toughness for total joint arthroplasty [6–9], or as highly porous constructs used in bone scaffolds and arthrodesis devices [10–12]. Si_3N_4 is biocompatible [13–19], exhibits excellent
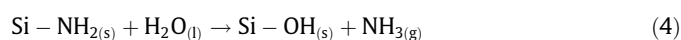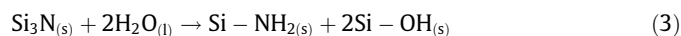
---

* Corresponding author.
E-mail address: rbock@amedica.com (R.M. Bock).

radiographic visibility as a partially-radiolucent material [4,20,21], and has decreased bacterial activity compared to polyetheretherketone (PEEK) and titanium [22,23]. Si_3N_4 was first used as a spinal implant in a small clinical trial in Australia in 1986 [17]. However, since 2008, it has been routinely used as spinal fusion cages, with in excess of 24,000 implantations to date and few reported adverse events [24]. Dense, highly polished bearings made from Si_3N_4, for potential use in total joint arthroplasty, have also been developed and tested [4,25,26], although they are yet to be cleared for this purpose by regulatory agencies.
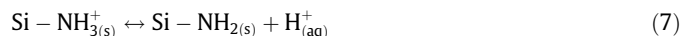
Much like native metal surfaces, Si_3N_4 develops a surface passivation layer due to its thermodynamic instability in oxidizing or moist environments, which has been directly observed to be $\sim$3–5 nm in thickness [27]. The reactions governing its formation are given by the following equations [28]:

$$Si_3N_{4(s)} + 3O_{2(g)} \rightarrow 3SiO_{2(s)} + 2N_{2(g)} \qquad \Delta G \; 298 \, °K = -1922 \, \frac{kJ}{mol}$$
(1)

$$Si_3N_{4(s)} + 6H_2O_{(l)} \rightarrow 3SiO_{2(s)} + 4NH_{3(g)} \qquad \Delta G \; 298 \, °K = -565 \, \frac{kJ}{mol}$$
(2)

However, the surface chemistry of Si_3N_4 is more complex than these equations would indicate because the near-surface region is composed of Si–N, Si–N–O, and Si–O bonds [27,29–33]. Its composition transitions from nearly pure Si–N in the bulk, to intermediate Si–N–O, and finally Si–O as the oxide layer thickens, becoming chemically equivalent to silica (SiO_2) at the surface. When exposed to air or moisture, Si–N bonds, predominately as $\equiv Si_3N$, react to form both charged (Si–NH_3^+, Si–OH_2^+, Si–O^-) and neutral (Si–NH_2, Si–OH) functional groups [30,34–37]. Accepted forms of the chemical reactions that produce these surface moieties are [30,35]:

$$Si_3N_{(s)} + 2H_2O_{(l)} \rightarrow Si - NH_{2(s)} + 2Si - OH_{(s)}$$
(3)

$$Si - NH_{2(s)} + H_2O_{(l)} \rightarrow Si - OH_{(s)} + NH_{3(g)}$$
(4)

The existence of these on-going reactions is readily apparent to those who work with finely divided Si_3N_4 powders due to the pungent presence of ammonia gas. In water, the predominant functional groups, Si–NH_2 and Si–OH, dissociate via acid-base reactions as follows [35,38,39]:

$$Si - OH_{2(s)}^+ \leftrightarrow Si - OH_{(s)} + H_{(aq)}^+$$
(5)

$$Si - OH_{(s)} \leftrightarrow Si - O_{(s)}^- + H_{(aq)}^+$$
(6)

$$Si - NH_{3(s)}^+ \leftrightarrow Si - NH_{2(s)} + H_{(aq)}^+$$
(7)

The protonation of a silanol group (Eq. 5) is unlikely to occur except in highly acidic environments, leaving Eqs. (6) and (7) as the principal reactions at homeostatic pH. These reactions can be driven forward or backward by manipulating the pH of the environment (*i.e.*, changing the concentration of H$^+$ and/or OH$^-$). The pH at which a material displays zero net surface charge is its isoelectric point (IEP), and is indicative of an equal balance of positively- and negatively-charged surface sites [40]. At a pH greater than the IEP, a material will exhibit net negative charge, while the opposite occurs at a pH below its IEP. Surface charging is often characterized via indirect measurement of zeta potential (ζ-potential, or ζ) in the case of fine particulate matter, or streaming potential in the case of bulk surfaces [41]. Pure Si_3N_4 has an IEP of $\sim$9.3–9.7 owing to the high concentration of amine (Si–NH_2) sites on its surface [31,42]. Since the amine sites are not readily reduced, a negative surface charge is seldom observed on pure

Si_3N_4. Conversely, pure SiO_2 exhibits an isoelectric point of 2–3 owing to the highly-favorable surface reduction reaction (Eq. (6)) [43]. It has been shown that Si_3N_4's IEP will shift from that of the pure nitride ($\sim$9) to that of pure silica ($\sim$2) as the surface oxide layer thickens [31,37]. Therefore, measuring the IEP of a Si_3N_4 material is one method to estimate oxide layer thickness and the balance between surface amine and silanol groups.

While extensive surface characterization of α-Si_3N_4 particles [27,30,31,33,37], Si_3N_4 films [29,44], and β-Si_3N_4 whiskers [45,46], has been performed, few data are available for the type of material used in this study – a bulk β-Si_3N_4 doped with alumina (Al_2O_3) and yttria (Y_2O_3). The Al_2O_3 (5.5 mol percent) and Y_2O_3 (3.7 mol percent) are added as sintering aids.

Si_3N_4 has been historically difficult to densify without employing additives, typically either magnesia (MgO) or a mixture of Al_2O_3 and Y_2O_3 [7,8,47]. During sintering, these additives react with Si_3N_4 and residual SiO_2 to form a liquid phase. Upon cooling, the liquid solidifies as either an intergranular glass or crystalline silicon yttrium aluminum oxynitride (SiYAlON). Liquid phase sintering allows for engineering of Si_3N_4's microstructure for improved fracture toughness by dissolution of isotropic α-phase Si_3N_4 particles which then precipitate as elongated β-phase grains. These elongated grains are oriented stochastically and enable interface debonding and crack bridging mechanisms responsible for a crack-length dependent toughness increase [7–9,47]. The presence of these additives further convolutes Si_3N_4's surface chemistry due to formation of hydrolyzed Al–OH and Y–OH functional groups at regions where grain boundaries intersect the exposed surface. Charging of these sites in an aqueous environment occurs similarly to Si–OH as follows [39]:

$$Y - OH_{2(s)}^+ \leftrightarrow Y - OH_{(s)} + H_{(aq)}^+$$
(8)

$$Y - OH_{(s)} \leftrightarrow Y - O_{(s)}^- + H_{(aq)}^+$$
(9)

$$Al - OH_{2(s)}^+ \leftrightarrow Al - OH_{(s)} + H_{(aq)}^+$$
(10)

$$Al - OH_{(s)} \leftrightarrow Al - O_{(s)}^- + H_{(aq)}^+$$
(11)

IEPs for the dopants have been reported to be $\sim$8–9 for Y_2O_3 [48], $\sim$9 for α-Al_2O_3 [43,48,49], and 6–7 for a silica-rich silicon oxynitride [50]. The IEP of the intergranular glass likely lies somewhere in-between, and will skew the material's IEP relative to pure Si_3N_4 accordingly. The material's phase composition, essentially 100% β-Si_3N_4 for the material studied here, and exposed crystallographic habit also influence surface chemistry (with respect to amine and silanol functional sites) due to the concentration and spacing of exposed surface atoms. As a result of a combination of these phenomena, Si_3N_4 immediately develops a surface charge when placed in a biological environment, and is covered by a layer of ions and proteins. Furthermore, it is well-known that topography plays a significant role on the formation of this adsorption layer and, thus the response of cells *in vitro* and *in vivo* [51–56]. For instance, texturing has been employed as a means to improve bone growth onto titanium [52,54], and certain metal oxide passivation layers have demonstrated direct bone on-growth [53,55]. Surface composition also has an effect. Complex interactions are observed for certain resorbable materials (*e.g.*, hydroxyapatite, bioglass, etc.) which promote bone growth [54,56,57]. Hydroxylated surfaces of TiO_2, Ta_2O_5 and SiO_2 have been shown to induce apatite formation at biologic pH both *in vitro* and *in vivo* [58,59] through a proposed mechanism that relies upon the material's surface exhibiting negative charge at homeostatic pH. Additionally, attraction and adhesion to surfaces by bacteria and other cells have been interpreted using the so-called extended Derjaguin and Landau, Verwy and Overbeek (DLVO) theory [60,61] which accounts for

additional interactions, such as hydrogen bonding, in addition to van der Waals and double layer interactions as described by traditional DLVO theory [40,62,63]. Understanding of charging behavior and other surface chemical properties engendered by processing and subsequent surface treatment will enable a mechanistic evaluation of anti-bacterial and osteointegration behaviors. Once the root mechanisms of these behaviors are understood, the material's surface can be engineered for resistance to bacterial colonization, osteointegration, or other application-specific properties.

Si_3N_4 produced by reaction bonding, which contained little or no additives, demonstrated excellent biocompatibility and bone on-growth *in vivo* using a rabbit model [14]. Si_3N_4 containing Al_2O_3 and Y_2O_3 in similar concentrations to the material studied here exhibited no cytotoxic response in *vitro* [2] and excellent bone on-growth with no observed adverse effects in an *in vivo* rabbit model [19]. Furthermore, Si_3N_4 processed in an identical manner to the material studied here exhibited decreased surface bacterial activity *in vitro* [22], and favorable osteointegration, resistance to bacterial colonization, and no evidence of cytotoxicity in an *in vivo* rat model [23].

The present study was undertaken for multiple reasons: (1) to gain a deeper understanding of the composition, structure, and properties of Si_3N_4 surfaces; (2) to explore and characterize extreme surface compositions achievable with conventional thermal, chemical, and mechanical treatments (*i.e.*, to maximize surface hydroxyl groups through oxidation or to conversely maximize the available surface amine groups through HF etching or heating in a nitrogen atmosphere); and (3) to lay a foundation for future studies that will explore mechanistic relationships between exhibited surface properties and previously-observed anti-infective and osteointegrative behavior.

2. Materials and methods

2.1. Silicon nitride material and sample preparation

The Si_3N_4 used in the present study was produced by Amedica Corp., (Salt Lake City, UT), using conventional ceramic fabrication techniques. In this process, Si_3N_4 powder (Ube SN E-10, Ube City, Japan) was mixed with Y_2O_3 (Grade C, H. C. Starck, Munich, Germany) and Al_2O_3 (SA8-DBM, Baikowski/Malakoff, Charlotte, NC) sintering aids and formed at room temperature into a green body with the required geometry. The green body was then sintered in a nitrogen atmosphere at a temperature in excess of 1700 °C to closed porosity and further densified by hot isostatic pressing at a temperature exceeding 1650 °C and N_2 gas pressures of >200 MPa. The resulting Si_3N_4 exhibited a two-phase microstructure consisting of anisotropic β-Si_3N_4 grains separated by thin (<2 nm) grain boundaries of amorphous or crystalline yttrium aluminum oxynitride or Si(Y)AlON, respectively [64].

The as-fired Si_3N_4 was divided into two groups. One group was sectioned into wafers (10 mm × 10 mm × 2 mm) with one major face left as-fired and the remaining faces ground flat using a 1000 grit diamond-impregnated wheel on a surface grinder (ACC 12-24DX Grind-X, Okamoto Corp., Vernon Hills, IL). This sample group was designated "as-fabricated." The second group was sectioned into wafers of the same geometry with all six faces ground to the same finish. One of the major faces on each wafer was lapped using 6 μm diamond (Engis, Wheeling, IL) on a lapping machine (Lapmaster, Mt. Prospect, IL), and subsequently polished using colloidal silica (Leco, St. Joseph, MI). This group was designated "as polished." Both wafer groups (as-fabricated and as-polished) were subjected to ultrasonic cleaning in deionized water of 17.5 MΩ cm resistivity (750II, Myron L Company, Carlsbad, CA) for 30 min to remove contaminants. The wafers were then divided

into sub-groups and subjected to the thermal and chemical treatments described in Section 2.2.

Samples were prepared with modified geometries for Raman spectroscopy, streaming potential and wetting angle measurements. Rectangular plates with dimensions of 40 mm × 20 mm × 1 mm were used for streaming potential measurement, and circular discs of Ø12.7 mm × 3 mm were used for Raman spectroscopy and wetting angle determinations. Aside from deviations in dimensions, the preparation of all samples was identical to that described above.

2.2. Surface treatment methods

Wet Chemical Etching – It is well-documented that hydrofluoric acid (HF) can be employed to etch both SiO_2 and Si_3N_4 surfaces [65–67]. The removal rate of SiO_2 tends to be significantly faster (1–2 orders of magnitude) than that of Si_3N_4. This allows for removal of the SiO_2 passivation layer without significantly etching the underlying nitride. It was anticipated that this treatment should maximize the concentration of amine groups at the surface by etching away the passivation layer, thus pushing the surface composition as far to the nitride end of the nitride-oxide spectrum as possible. Samples were immersed in a 5 wt.% HF solution for 45 s, transferred into a continuously refreshed DI water bath for 30 min, dried under a stream of filtered N_2, and stored in a desiccator containing hygroscopic media (Indicating Drierite, W.A. Hammond DRIERITE Co., Xenia, OH) under partial vacuum (∼100 Torr) to slow spontaneous re-oxidation.

Nitrogen Heat Treatment – It was hypothesized that re-exposing Si_3N_4 to a N_2 atmosphere at high temperatures might increase the density of surface amines relative to hydroxyl groups. As a result, this heat treatment was seen as a potential alternative to the HF etching treatment. Samples were placed in a batch furnace (Centorr Vacuum Industries, Nashua, NH), evacuated to 250 mTorr, then back-filled with filtered N_2 (1–2 psi) and subsequently heated to 1400 °C for 30 min.

Oxidation Treatment – Raider et al. demonstrated that chemical vapor deposited (CVD) Si_3N_4 is readily oxidized upon exposure to ambient atmosphere at 1070 °C [29]. A study by Butt et al. showed similar results for two commercially-produced Si_3N_4 powders [32]. This treatment was employed because it was believed that it should completely oxidize the surface, yielding the maximum concentration of hydroxyl groups and pushing the surface composition as far to the oxide end of the nitride-oxide spectrum as possible. The 7 h dwell at 1070 °C employed by Raider et al., which was shown to completely oxidize the studied CVD Si_3N_4 sample's surface, was adopted for oxidizing samples using an open-air kiln (Deltech, Denver, CO).

2.3. Sample characterization methods

Scanning Electron Microscopy (SEM) – SEM studies were carried out using a field emission gun scanning electron microscope (FEG-SEM) (Quanta, FEI, Hillsboro, OR). All samples were sputter-coated (108auto, Cressington, Watford, UK) with a thin (∼20–30 Å) layer of gold. Samples were imaged using an accelerating voltage of 10 kV at working distances of 7–10 mm and spot sizes of 4–4.5 mm.

Atomic Force Microscopy (AFM) – Two- and three-dimensional images, and roughness values (average and root mean square) of each sample were obtained using an AFM (Nanoscope IIIa; Veeco Instruments Inc., Plainview, NY) over the maximum $x–y$ range available with the instrument (∼13 μm).

X-ray Photoelectron Spectroscopy (XPS) – A spectrometer (Axis Ultra, Kratos, Manchester, UK) was employed with an Al-kα monochromatic X-ray source. Low resolution spectrum scans were

conducted using a pass energy of 160 eV, with a compositional resolution of approximately 0.1 atomic percent (at.%). High resolution scans bracketing peaks of interest were conducted using a pass energy of 40 eV, which was expected to improve the compositional resolution to approximately 0.01 at.%. The analysis area was set to the spectrometer's maximum (700 μm × 300 μm) in order to average out differences between the composition within grains and the intergranular phase. Data obtained were processed using commercially-available software (CasaXPS, Casa Software Ltd., UK). Usage of a low energy electron source and application of ultra-high vacuum-rated colloidal silver (Ted Pella, Inc., Redding, CA) to the contact points between the samples and the fixture were employed to mitigate charging effects. All reported data were obtained following argon sputtering to remove adsorbed surface contaminants, at a beam energy of 4.2 keV, gun angle with respect to sample of 45°, raster area of 3 mm × 3 mm, and a sample current of approximately 2 μA.

Wetting Angle Measurements – An optical comparator (2600 Series, S-T Industries, St. James, MN) with built-in goniometer functionality was used to measure static contact angles of deionized water droplets having fixed volumes (VWR Signature Variable Volume Pipette, VWR, Radnor, PA) of 25 μL. Both sides of each droplet's projected image were measured, and at least eight measurements were taken per condition. In the case of untreated, as-fabricated Si_3N_4, iterative measurements of the deposited droplets were carried out over a period of 30 min in an effort to characterize the transition from Cassie–Baxter to Wenzel states [68].

Zeta Potential Measurements – Streaming potential measurements were performed using an electrokinetic analyzer (SurPASS, Anton-Paar USA, Ashland, VA). A background electrolyte of 1 mM HCl, which exhibited a natural pH of 5.5, was used in all experiments. Experiments were divided into two runs. The first run took measurements across a pH range of 5.5–3 using auto-titration of 0.1 M HCl solution to control pH. The second run used a new solution of background electrolyte for measurements across a pH range of 5.5–10 and auto-titration of 0.1 M NaOH solution to control pH. Each run contained two material samples. Observed streaming potentials were converted to zeta potentials using the Helmholz-Smoluchowski equation [41].

Raman Spectroscopy – Raman spectra were acquired using a confocal (optical) microprobe at room temperature and a single monochromator (T-64000, Jobin-Yvon/Horiba Group, Kyoto, Japan) equipped with a nitrogen-cooled 1024 × 256 pixels CCD camera (CCD-3500V, Horiba Ltd., Kyoto, Japan), and analyzed by using commercially available software (LabSpec, Horiba/Jobin-Yvon, Kyoto, Japan). The excitation frequency used in the experiment was the 532 nm blue line of an Ar-ion laser operating at a power of 100 mW. The spectrum integration time was typically 30 s, averaging the recorded spectra over three successive measurements. A confocal configuration of the Raman probe was adopted throughout all the experiments, using a 100× objective lens in order to exclude the photons scattered from out-of-focus regions of the probe. The samples were placed on an x–y axes motorized stage (lateral resolution of 0.1 μm), which allowed the collection of maps on the surface. Moreover, finely tuned z-axis displacements allowed the collection of spectra at different depths. A signal from a He-Ne lamp was collected throughout all measurements as an internal reference for Raman peak positions. Raman band parameters were obtained through fitting the raw experimental spectra with Lorentzian curves.

Laser-Scanning Microscopy – Micrographs of the selected surfaces were collected by means of a 3D laser-scanning microscope (VK-X200K Series, Keyence, Osaka, Japan) using a 150× objective lens, with a numerical aperture of 0.9. The supplied software allowed the calculation of the surface roughness according to ISO 4287:1997.

3. Results

Surface Topography – Fig. 1 provides SEM images of the various treated Si_3N_4 samples. The as-fabricated material exhibited classic protruding anisotropic, hexagonal β-Si_3N_4 grains (Fig. 1a). A representative cross-section of this microstructure as imaged using a back-scatter detector is given in Fig. 1b, which shows the presence of the Y_2O_3- and Al_2O_3-rich intergranular phase. When the as-fabricated material is etched in HF (Fig. 1c), the overall topography is similar to the untreated case (Fig. 1a) with the exception of etching damage at the tips of many grains (indicated by white arrows). The morphology of the as-fabricated surface following the nitrogen heat treatment (Fig. 1d) appears similar to as-fabricated samples with the exception of fine particulates between some grains. These particulates exhibited a much higher average atomic mass than Si_3N_4. Similarly, a back-scatter image of polished specimens subjected to the same thermal treatment in N_2 (Fig. 1e) shows the presence of a new phase, also having a higher average atomic mass, and an absence of the intergranular phase. Finally, specimens subjected to the oxidation treatment (Fig. 1f) show a second phase (assumed to be the oxide layer), which covers and spans the grains. AFM images confirmed large difference in surface topography between as-fabricated and polished samples (Fig. 2). On the other hand, no marked differences were found among AFM images for as-fabricated, thermally treated, and HF treated groups. As expected, roughness (R_a) values determined from AFM showed marked differences between chemical mechanical polished (CMP) and as-fabricated surfaces (cf., Table 1). However, small differences were noted among treated and as-fabricated surfaces. In general, the as-fabricated and HF-treated samples had higher R_a values than either of the thermally treated materials.

X-ray Photoelectron Spectroscopy – XPS showed major differences in surface composition among the treatment conditions (cf., Table 2). The as-fabricated Si_3N_4 had N/Si and O/Si atomic ratios of 1.01 and 0.49, respectively. These ratios corresponded closely to silicon oxynitride (Si_2N_2O). In comparison, samples thermally-oxidized in air exhibited a composition that corresponded to SiO_2. When compared to as-fabricated Si_3N_4, samples etched in HF or subjected to CMP had higher N/Si and lower O/Si atomic ratios. Subjecting the polished sample to etching in HF resulted in little alteration. Except for a higher amount of Al and Y, the sample thermally treated in N_2 showed a surface composition that appeared similar to that of the as-fabricated material. In general, the surface of the thermally treated samples had higher concentrations of Al and Y when compared to samples that were not thermally treated. The C (1s) peak in the spectra was likely due to trace hydrocarbons in the spectrometer, impurities resulting from the post-fabrication processing, or both. Trace amounts of elements found in the spectra, such as Na, Mg, Fe, and Ca, were presumably present because of surface contamination.

Wettability and Contact Angle – The deionized water contact angle on the CMP surface (47 ± 3°) was significantly lower than the as-fabricated surface (66 ± 12°), or the surface subjected to etching in HF (60 ± 13°). Thermal treatments of as-fabricated specimens produced extremely low contact angles (cf., Table 3), either in air (8 ± 1°) or nitrogen (9 ± 2°). In the case of the as-fabricated samples, droplets were measured at several intervals over a period of 30 min following deposition. The contact angle on the as-fabricated material was found to decrease from 66 ± 12° at deposition to 30 ± 9° after 30 min (cf., Table 4).

Zeta-Potential – Fig. 3a shows the ζ-potential as a function of pH for as-fabricated Si_3N_4 in an unmodified state, after HF-etch, and following thermal oxidation, with IEPs of 4.5, 4.7, and 3.1, respectively. All had negative ζ-potentials of −45 mV, −50 mV and −70 mV at homoeostatic pH of ∼7.4, respectively. Fig. 3b
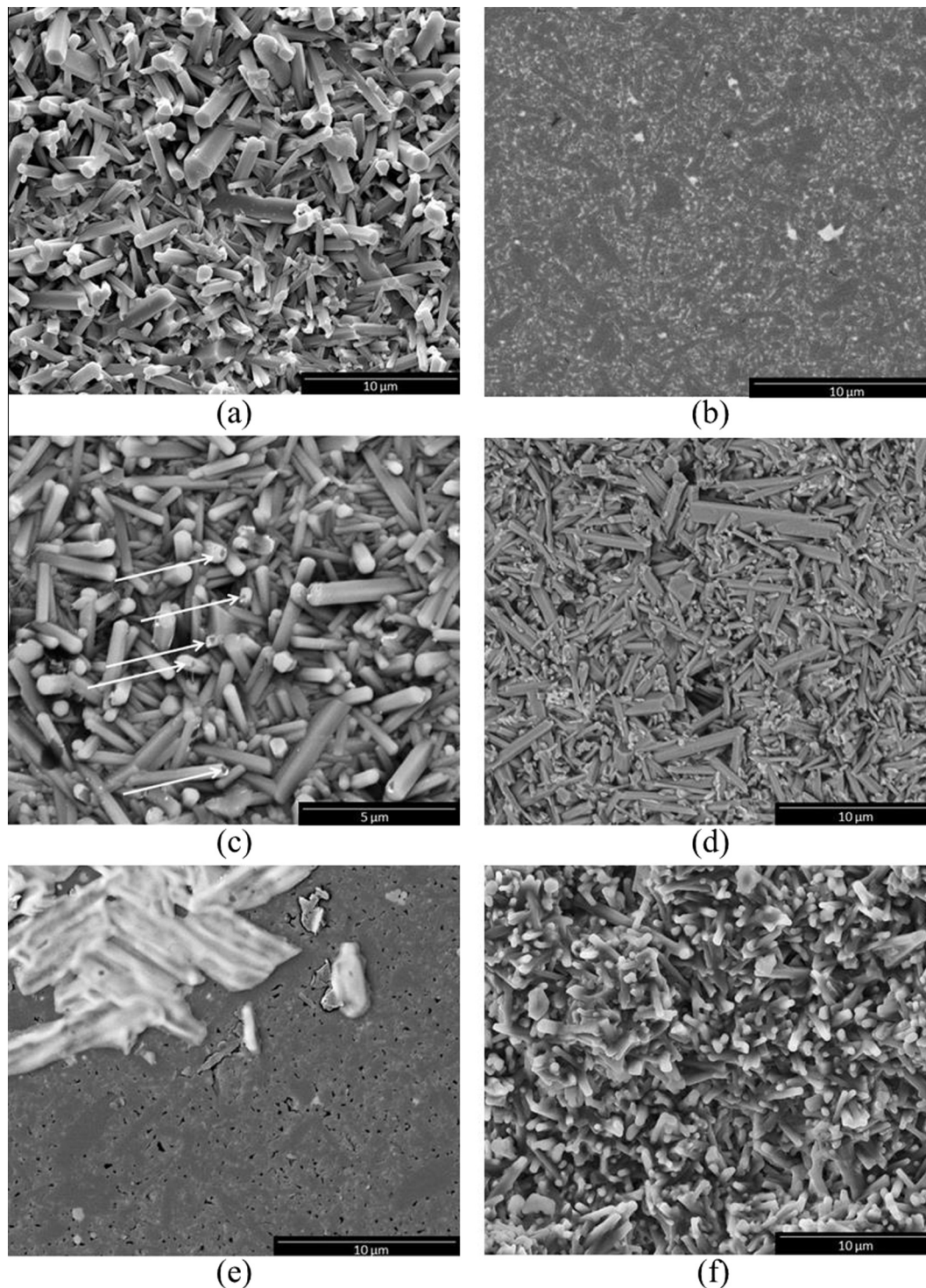
Fig. 1. Electron photomicrographs of Si_3N_4 surfaces subjected to varying surface preparations. (Images are secondary electron photos unless otherwise specified). as-fabricated (a), chemical mechanical polished (back-scatter) (b), HF etched (back-scatter) (c), 1400 °C for 30 min in N_2 (back-scatter) (d), chemical mechanical polished followed by 1400 °C for 30 min in N_2 (back-scatter) (e), and 1070 °C for 7 h in air (f).

provides similar ζ-potential data for CMP specimens. The as-polished, HF-etched, and oxidized samples exhibited IEPs of 5.6, 5.4 and $\sim$2, respectively; with negative ζ-potentials of -45 mV, -40 mV and -120 mV at homeostatic pH, respectively.

Raman Spectroscopy – Fig. 4(a) through (d) show the Raman spectra collected on the polished surfaces of different Si_3N_4 samples in the 150–250 cm^{-1} region (untreated, HF-etched, treated in N_2, and treated in air, in (a), (b), (c), and (d), respectively). The

figure also shows fits of the triplet into sub-bands obtained using pure Lorentzian curves as trial functions. A line map along the z-axis, (i.e., with defocusing below the free surface of the sample), is shown in Fig. 5. The doubled triplet tended to disappear with focusing below the free surface.

Laser-Scanning Microscopy – Laser micrographs of the polished surface in untreated, N_2, and air-treated states are shown in Fig. 6 (a–c), respectively. As seen in the micrographs, the thermally
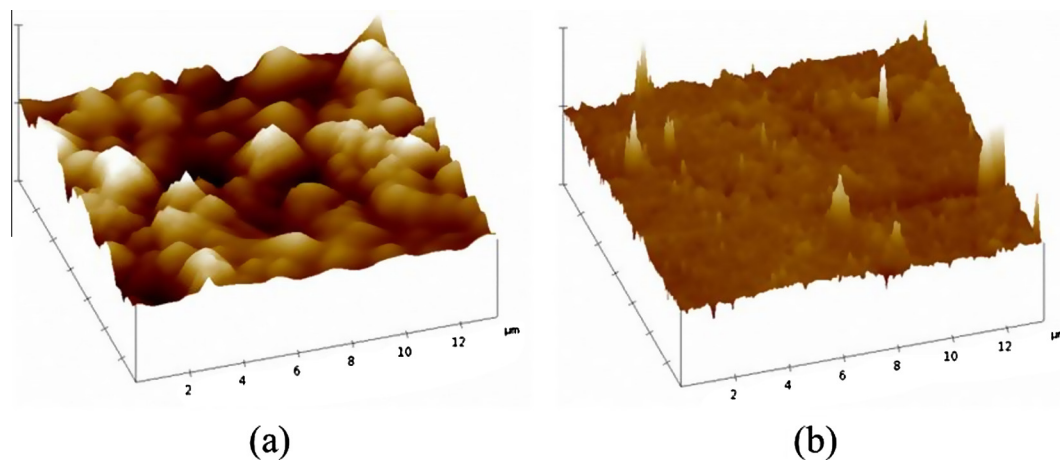
Fig. 2. AFM images of the surface of the as-fabricated Si₃N₄ (a), and after chemical mechanical polishing (b). The peaks in (b) are presumably due to residual particles from the polishing.

Table 1
Summary of the roughness average (R_a) and the root-mean-square roughness (R_q) of the Si₃N₄ materials.

Sample	R_a (nm)	R_q (nm)
As-fabricated	336	433
Thermal treatment in air	287	369
Thermal treatment in N₂	296	373
Etched in HF	341	439
Chemical mechanical polished	9	16

treated samples show a different texture as compared to the untreated surface, which is especially marked after the N₂ thermal treatments.

4. Discussion

Surface Topography – The as-fabricated Si₃N₄ samples exhibited a surface roughness (R_a) of 336 nm, but this was reduced to <10 nm after CMP. HF etching of as-fabricated samples had little effect on roughness, presumably because only the thin SiO₂ layer on the protruding grains was removed. Thermal treatments in air or N₂ resulted in a reduction in R_a to 287–296 nm due to formation of oxidation products in the valleys between grains (in air) or migration of the grain boundary phase to the surface (in air or N₂). The presence of an oxidized phase or particulates between protruding

Table 2
Concentration (in atomic %) of the major and minor elements on the surface of the Si₃N₄ samples and their respective calculated N/Si and O/Si atomic ratios. The theoretical composition based on the batch recipe is also included for comparison purposes.

Sample	Concentration (at.%)						Atomic ratio	
	Si	N	O	Al	Y	C	N/Si	O/Si
Theoretical bulk composition	39.7	52.9	4.5	1.6	1.1	–	1.33	0.11
As-fabricated	35.1	35.5	17.5	2.1	0.1	9.7	1.01	0.49
HF-etched	31.6	35.2	8.4	0.9	0.1	21.8	1.12	0.27
Thermal treatment in N₂	32.7	33.3	16.6	5.1	2.1	10.3	1.02	0.50
Oxidized	32.7	0.1	57.7	2.9	1.3	5.4	0.00	1.76
Chemical mechanical polished	38.7	47.2	6.4	1.6	0.8	5.3	1.22	0.17
Polished & HF-etched	42.1	44.2	6.2	1.8	0.6	5.3	1.05	0.15
Polished & oxidized	27.6	2.5	54.6	3.9	4.6	6.6	0.09	1.98

Table 3
Sessile drop contact angle (θ) of deionized water on the surface of treated Si₃N₄ materials.

Sample	θ (°)
As-fabricated	66 ± 12
Chemical mechanical polished	47 ± 3
As-fabricated, etched in HF	60 ± 13
As-fab, thermal treatment in N₂	9 ± 2
As-fab, thermal treatment in air	8 ± 1

Table 4
Sessile drop contact angle (θ) of deionized water on the surface of as-fabricated Si₃N₄ over a duration of 30 min.

Time (min)	θ (°)
0	66 ± 12
5	59 ± 12
15	48 ± 10
20	41 ± 11
25	35 ± 13
30	30 ± 9

grains in the thermally treated samples was confirmed by SEM (cf. Fig. 1d–f) and by morphological differences on polished surfaces (cf. Fig. 7b and c). The as-fabricated, HF-etched and thermally treated Si₃N₄ samples showed columnar surface microstructures composed of anisotropic grains oriented stochastically (cf. Fig. 1). Smooth surfaces are required for bearings in hip and knee arthroplasty because conforming surfaces result in higher contact area between components and hence lower stresses and wear rates. In contrast, surface roughness can markedly influence the response of cells in vitro and in vivo for implants intended for osseointegration and bacteriostasis. These features may elicit a different response when compared to a smoother undulating surface with the same R_a value. Indeed, bacterial resistance has been noted for materials that have similar asymmetric surfaces containing periodic protrusions [69].

X-ray Photoelectron Spectroscopy – The XPS data (Table 3) indicate that thermal, mechanical and chemical treatments induced significant changes in surface chemistry, producing a wide range of nitride/oxide atomic ratios, and increased concentration of sintering aids at the material's surface. Within the spectrometer's probe depth of up to ~2–3 nm [70], the surface composition of as-fabricated Si₃N₄, having a N/Si and O/Si atomic ratio of 1.01 and 0.49, respectively, appears to be silicon oxynitride, Si₂N₂O,

indicating the surface is partially-oxidized. It is comparable to Si_2-$N_2O_{0.8}$ found previously for a commercial Si_3N_4 powder [27]. There is likely a gradient in chemical composition, with decreasing oxygen away from the surface, as found for oxidized Si_3N_4 films [29]. In addition, minor amounts of Al and Y were also detected by XPS. Some of the oxygen on the surface is obviously bound to these elements instead of Si. Etching of as-fabricated Si_3N_4 in HF resulted in dissolution of this thin oxynitride layer. However, the etched surface will re-oxidize in air at room temperature, resulting in an oxide or oxynitride layer which increases in thickness over time [33]. When compared to as-fabricated Si_3N_4, the HF-etched surface showed higher N/Si and lower O/Si ratios as expected. The grain boundary phase is obscured by protruding grains on the as-fabricated samples. Therefore, it is not unexpected to see skewed

concentration values for sinter aid cations such as aluminum and yttrium, which segregate at the grain boundaries. CMP removed the entire surface layer from as-fabricated Si_3N_4. Further, the grain boundaries tended to recede during CMP due to a higher removal rate for SiO_2 relative to Si_3N_4 [67]. As a result, the polished surface showed the highest N/Si and lowest O/Si ratios. Also, Y_2O_3 exhibits increased solubility at elevated pH values, such as the pH 10–11 environment of the CMP slurry during the polishing process, which could contribute to its modestly lower than expected observed concentration. Due to sample handling in air. It is also likely that some re-oxidation occurred prior to conducting the XPS measurements. Therefore, it is believed that HF-etched and CMP-finished samples should exhibit an even lower oxygen content and higher IEP than has been reported here. However, the values shown in
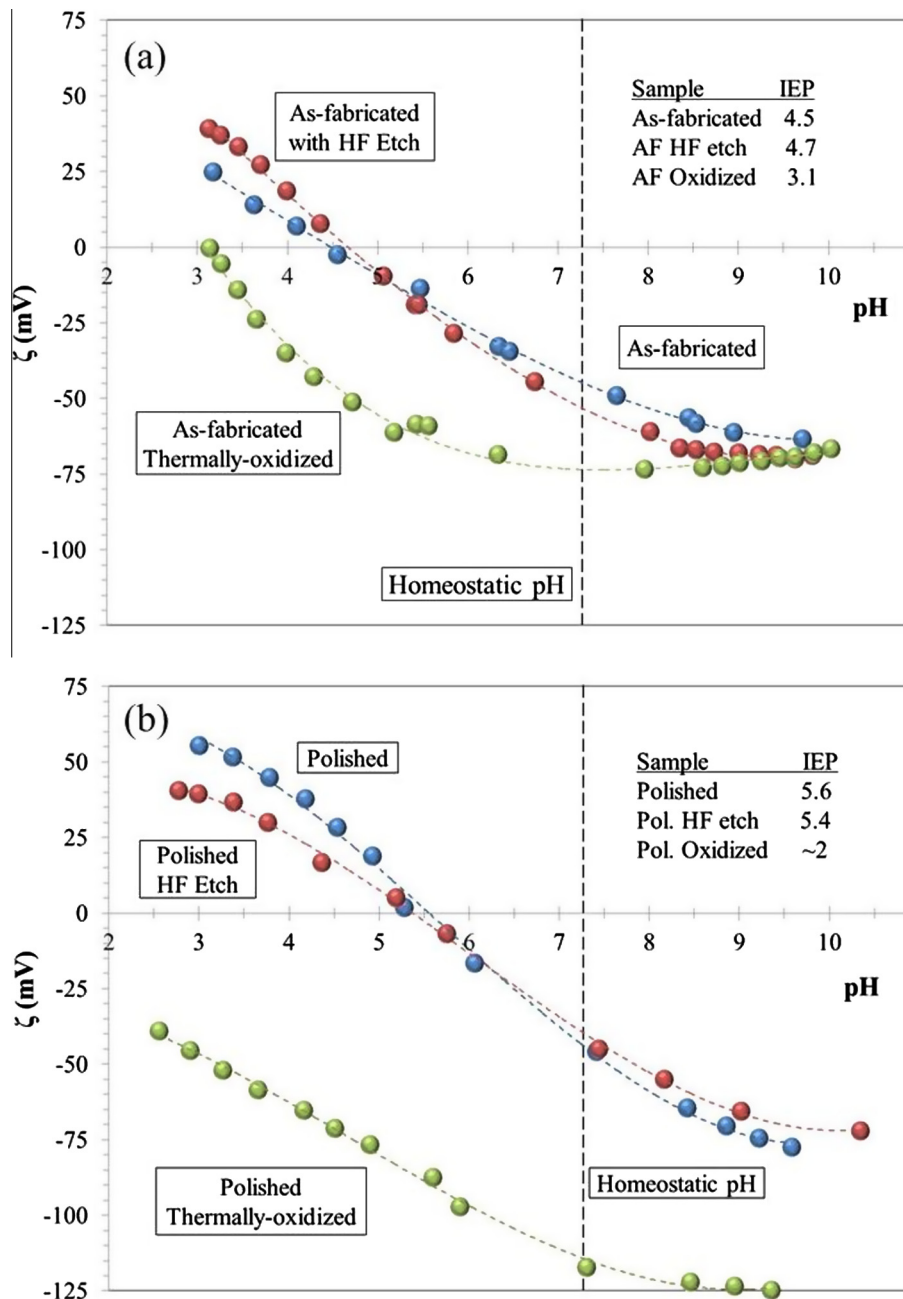

Fig. 3. Zeta potential as a function of pH, as measured by streaming potential, for as-fabricated Si_3N_4 (a), and for the Si_3N_4 after chemical mechanical polishing (b) for as-processed samples, samples exposed to an HF etch, and samples subjected to thermal oxidation in air.
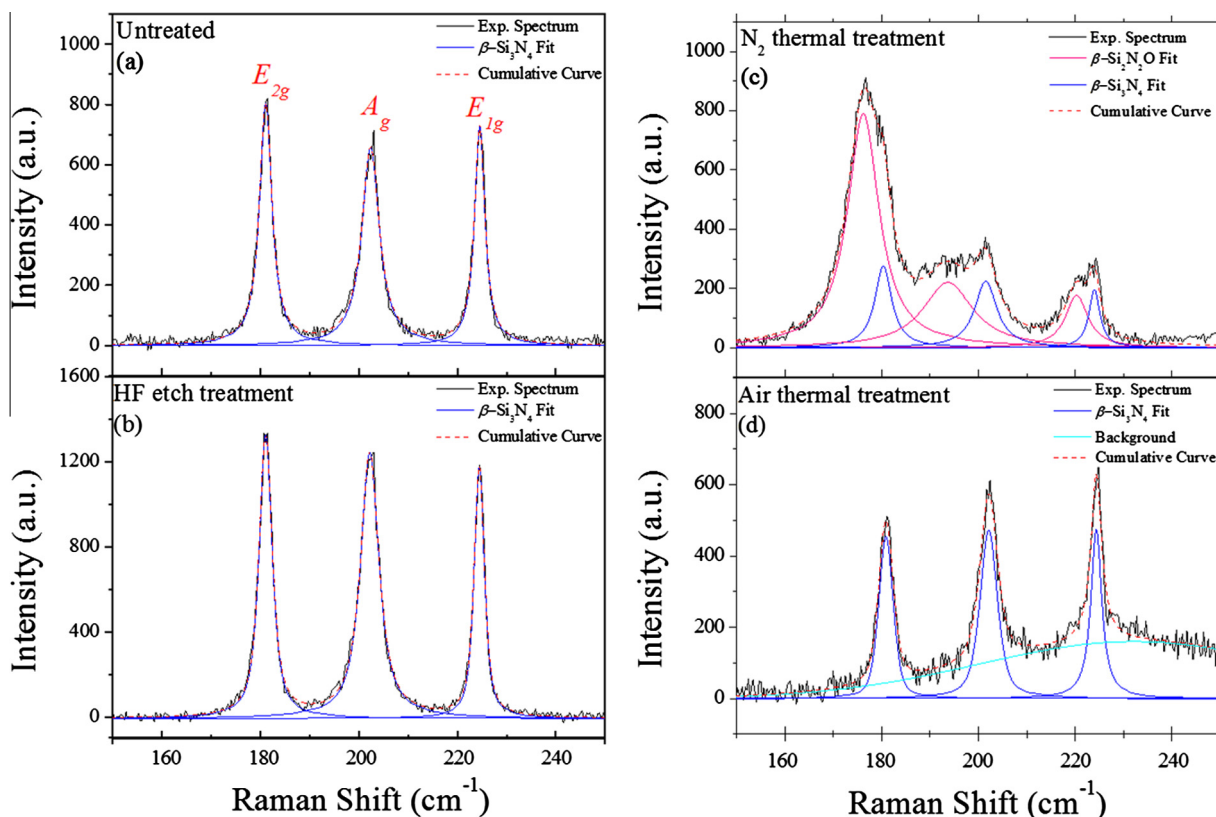
Fig. 4. Raman spectra of the β-silicon nitride surface in the 150–250 cm^{-1} region, as collected on the polished untreated sample (a), the sample etched in HF (b), the sample treated in N$_2$ (c) and that treated in Air (d). Sub-band fitting was obtained using Lorentzian curves.
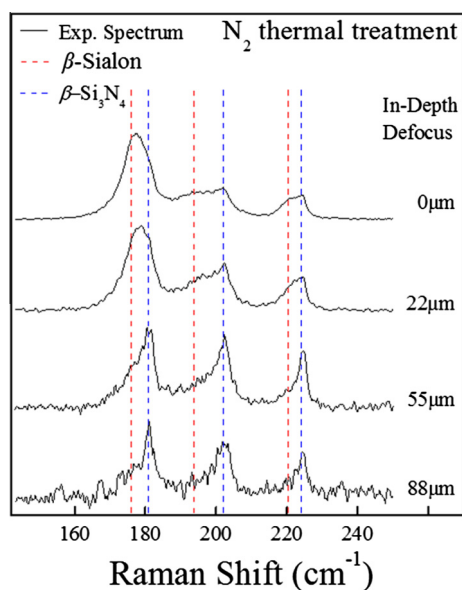

Fig. 5. In-depth profile of Raman spectra collected on the polished sample treated in N$_2$. Red and blue dashed lines indicate the position of the two triplets observed. The frequencies of the triplets have been chosen according to the fitting results shown in Fig. 4(b).

Table 2 are likely representative for limited handling of treated samples in air. Thermal oxidation of as-fabricated Si$_3$N$_4$ resulted in a surface composition corresponding to SiO$_2$. The amount of Al and Y, resulting from the intergranular phase, was also much higher than the as-fabricated Si$_3$N$_4$. This might be due to migration

of the grain boundary phase to the surface, as noted for other liquid-phase sintered Si$_3$N$_4$ ceramics [71–73]. In contrast, the surface composition of the Si$_3$N$_4$ thermally treated in N$_2$ showed little difference in N/Si and O/Si ratios from the as-fabricated material (*cf.*, Table 2), likely due to the thermal stability of the oxynitride layer in dry N$_2$. Yet, migration of the intergranular phase to the surface was observed as in the oxidation case. In this case, the migrated material manifested itself as fine particulates scattered between protruding surface grains, imaged using SEM (*cf.* Fig. 1d), and compositionally determined to contain Y and Al via XPS (*cf.* Table 1).

Zeta Potential – The surface treatments had a profound influence on surface charging. Chemical mechanical polishing of as-fabricated samples increased their isoelectric point from 4.2 to 5.5. The principle differences between as-fabricated and polished surfaces are: (1) an increase in exposed intergranular phase relative to grains; and, (2) a reduction in oxide layer thickness on the exposed grains. The intergranular phase is expected to exhibit a relatively high isoelectric point. Further, the reduction in the passivation layer thickness is expected to produce a more nitride-like surface, leading to an increase in the concentration of amine sites. Both of these changes are expected to shift the IEP higher, as was observed. Within the as-fabricated and as-polished groups, little difference was seen in charging behavior following etching in HF indicating that the as-fabricated and as-polished surfaces were minimally oxidized. Conversely, when these surfaces were oxidized, the result was a large shift in isoelectric point toward pure SiO$_2$ (pH 2). This behavior can be correlated with the N/Si and O/Si atomic ratios determined from the XPS data (*cf.* Table 2) and a broad peak corresponding to amorphous silica in the Raman spectrum (*cf.* Fig. 4d). Decreased O/Si and increased N/Si ratios increases the IEP. Previous studies have indicated the presence of silanol (Si–OH) and amine (Si–NH$_2$)
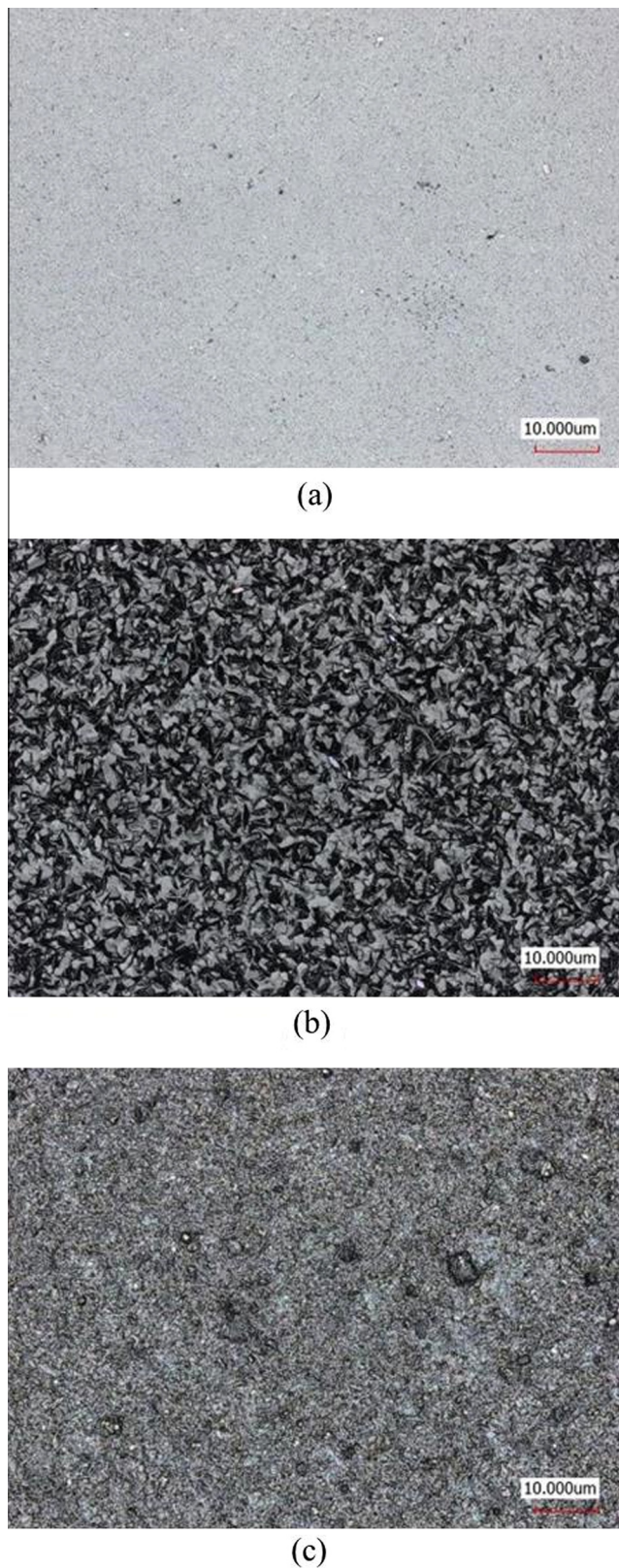
Fig. 6. Scanning laser micrograph of the Si₃N₄ surface (a) polished untreated, (b) thermally treated in N₂, and (c) thermally treated in air.

groups on the surface of Si₃N₄ powders [30,35,37]. Similar to observations of Greil et al., it is expected that the number of silanol groups correlates with the O/Si ratio, and the number of amine sites correlates with the N/Si ratio [37].

The mechanism for osteointegration proposed by Kokubo [58,59] for materials similar to Si₃N₄ relies upon negative surface charging at homeostatic pH. In studies using simulated body fluid, spontaneous deposition of apatite was observed on materials exhibiting a negative surface charge. Furthermore, *in vivo* studies using sample implants made from these same materials demonstrated formation of a morphologically similar apatite layer on implant surfaces and favorable osteointegration. It was hypothesized that the concentration of Ca^{2+} ions in the counterion cloud near the negatively-charged surface increased the local level of supersaturation of calcium-containing species, leading to precipitation of hydroxyapatite on the surface. As was observed here, Si₃N₄ exhibits a high negative surface charge. Therefore, it is possible that the favorable bone on-growth observed during a previous *in vivo* [23] study may be due at least in part to the mechanism proposed by Kokubo et al. Additional increases in the negative surface charge at homeostatic pH by oxidation of the material surface may accelerate apatite deposition. Modulation of charge magnitude may also allow for control of the deposited layer's morphology as a function of surface charge density by dictating the concentration and hence spacing of nucleation sites.

Consideration of bacterial attraction and adhesion using the extended DLVO theory [60,61] allows for understanding and testing of specific components of complex interactions between bacteria and the implant surface. As most bacteria exhibit a negative surface charge at physiologic pH [74–76], the electrostatic component of the cell-surface interaction will be repulsive if the implant material also exhibits negative charging. The magnitude of the repulsion will increase as the magnitude of the surface charge increases. The high negative surface charge on as-fabricated Si₃N₄ at physiologic pH observed here could contribute to the previously-observed bacteriostatic behavior of Si₃N₄ [22,23]. Furthermore, the ability to modulate the strength of this property through simple treatments allows for experiments to be devised for assessing its influence on the overall bacteria-surface interactions. The oxidized Si₃N₄ surface in particular, owing to its extreme negative surface charge, might provide an environment that inherently resists bacterial colonization.

Wettability and Contact Angle – A surface's chemistry and topography can strongly influence its wettability. The Wenzel equation describes the effect of a surface's roughness on wetting behavior [68]:

$$\cos\theta^* = r\cos\theta \qquad (12)$$

where θ^* represents the apparent equilibrium contact angle, r is the ratio of true surface area to apparent surface area, and θ is the contact angle for a flat surface. This equation predicts that increasing the roughness of a surface will lead to intensification of its observed wetting behavior, (*i.e.* a hydrophilic surface will become more hydrophilic, and a hydrophobic surface will become more hydrophobic). This was not directly observed in the cases of the as-fabricated and etched materials. These surfaces initially exhibited higher wetting angles (∼65°) than the polished surface (∼50°), which corresponded to heterogeneous behavior as described by the Cassie–Baxter equation [68]:

$$\cos\theta^* = r_f f\cos\theta + f - 1 \qquad (13)$$

where r_f corresponds to r in the Wenzel equation and f represents the fraction of the surface wet by the liquid. As more air is trapped at the solid–liquid interface, f decreases, and the apparent wetting angle increases. It should be noted that the CMP process produced a surface that is not substantially changed when subjected to HF etching (*cf.* polished sample XPS data in Table 2). The contact angle measurements presented here for polished surfaces were obtained within an hour of completing the CMP process, leaving little time for spontaneous re-oxidation. As such, the tested surface was lar-

gely devoid of oxygen and, as a consequence, silanol groups. In light of this, the wetting behavior was expected to be similar to historical HF etched Si_3N_4 thin films [77], and this was indeed the case. Furthermore, water contact angle measurements made on other similar polished Si_3N_4 materials varied between 46° and 61° [3]. Regarding the as-fabricated sample, the relatively high contact angle was likely due to fine gaps between the protruding grains on the surface. Water does not immediately infiltrate these gaps, leading to a mixed air/material interface (i.e., Cassie–Baxter behavior) [68]. However, the contact angle steadily decreased to ~30° within 30 min, which was significantly less than for polished samples. It is believed that this decrease was due to water slowly infiltrating the gaps between grains due to capillary forces in a process described as hemiwicking [78], thereby removing trapped air pockets from the interface. Contact angle measurements made previously on the same as-fabricated Si_3N_4 yielded a measurement of ~39°, which correlates with an intermediate time point in this study [23]. Droplets were observed to adopt ellipsoidal and other distorted semi-circular shapes instead of circles on as-fabricated and HF-etched surfaces. This is believed to be caused by variable amounts of trapped air at the solid–liquid interface as a result of the stochastic distribution of protruding grains. In cases where the surface roughness was reduced (i.e., N_2 and air thermal treatments, and polishing) there was less variation in wetting angles, and droplets adopted circular interfacial areas. As-fabricated samples subjected to thermal treatments displayed extremely low wetting angles (i.e., less than 10°). As shown via AFM (cf. Table 1) and qualitatively from electron micrographs (cf. Fig. 1(a, d and f)), the fine scale roughness of these samples was significantly reduced by their respective treatments. It is postulated that this reduction in roughness contributed, at least in part, to the occurrence of Wenzel behavior immediately upon wetting. That is, fine spaces between surface grains were likely filled by oxidation or migration of the intergranular phase, eliminating potential locations for air entrapment during wetting. The extremely low wetting angle following thermal treatment in air also correlates well with data obtained from streaming potential measurements. Thermally oxidized samples exhibited a much higher magnitude of surface charge at a pH near 7 than as-fabricated or HF-etched samples. Further, silica surfaces have been shown to exhibit low wetting angles [79]; so, it is not unexpected that the oxidized sample would also show better wetting. In a study examining techniques used to modify Si_3N_4 biosensor surfaces, Diao et al. [80] performed surface treatments to a CVD Si_3N_4 film, including HF-etching and oxidation. It was found that the HF etch process did not drastically alter the observed average water contact angle on the film surface (32° before and 33° after), but oxidation led to a drastic reduction in observed average water contact angle (to 5°). In light of this observation on relatively flat surfaces, it is thought that both the filling of fine intergranular spaces and the change in surface energy induced by the oxidation treatment contribute to the large observed change in water contact angle following oxidation in the present study. It was originally expected that samples etched in HF would exhibit significantly higher contact angles than their as-fabricated counterparts due to previous observations of HF-etch treatments on off-stoichiometry Si_3N_X thin films by Arafat et al. [77]. Large increases in water contact angles, attributed to surface hydrogenation, were found for these materials. However, relatively minor chemical changes (via XPS and Raman spectroscopy) and minimal variation in charging behavior (using streaming potential) were noted for as-fabricated and HF-etched conditions. Based upon these observations and those of Diao et al. on treated CVD Si_3N_4 films, similar wetting behavior between the two cases is not entirely surprising. It is also likely that some oxidation occurred during sample handling prior to characterization. The observed increase in hydrophilicity resulting from the

heat treatments in air and N_2 allows for more thorough wetting of an implant by body fluids. A modified Si_3N_4 surface that wets faster and more completely may also osteointegrate more effectively due to its greater area in contact with biologic fluids.

Raman Spectroscopy – The three intense bands (located at 180.1, 201.4 and 234.5 cm^{-1} in the as-fabricated sample) was observed in the Raman spectra of all samples (Fig. 4) and represent the E_{2g}, A_g, and E_{1g} vibrational modes of the skeletal Si–N bonds in the β-Si_3N_4 structure, respectively [81,82]. The as-fabricated and HF-treated samples presented quite similar Raman spectra (cf. Fig. 4(a and b), respectively). However, one clear difference in the relative intensity among bands belonging to the shown triplet could be detected: The HF treatment reduced the relative intensity of the A_g, band with respect to the E_{2g} and E_{1g} bands, whose relative intensity instead remained unchanged. In first approximation, this variance can be attributed to differences in crystallographic orientation of the surface crystallites irradiated by the incoming polarized laser. On the other hand, no significant broadening could be detected in any of the triplet constituents. The morphological changes observed in the Raman spectrum collected from the sample thermally treated in N_2 were by far more drastic (cf. Fig. 4(c)). One can still observe the original triplet belonging to the untreated sample, but also an additional triplet, significantly broadened and markedly shifted toward lower emission frequencies, could be observed. The sample treated in air did not show this additional (shifted) triplet (cf. Fig. 4(d)). However, it also showed distinct differences as compared to the untreated sample, as follows: (a) Besides a clear decrease in the absolute intensity of all bands constituting the triplet, the trend of relative intensities was inverted as compared to the untreated sample, with the intensity order becoming $E_{2g} < A_g < E_{1g}$; (b) Some broadening could be observed, but the spectrum could yet be deconvoluted into the main triplet of the untreated sample overlapped to a quite broad emission centered at approximately 230 cm^{-1}. This broad band can be interpreted as a low-frequency component of the overall broad Raman emission of silica glass [83]; and, (c) A small shift toward lower frequencies of the triplet could be found as compared to the standard positions recorded in the untreated sample. Broadening and shift of the skeletal triplet observed in the Raman spectra (Fig. 4) could be induced either by an internal (residual) stress state and related gradients [84–86], or by the development of different stoichiometric conditions [87], or both. Thermally induced residual stress of an elastic tensile nature might be responsible for the slight shifts observed in the sample treated in air as compared to the untreated one. However, the morphological differences detected in the N_2-annealed sample cannot only be due to internal stresses and have to be interpreted in terms of stoichiometry changes. Since the dimension of the Raman probe is far larger than that of the XPS one, care should be taken in extrapolating data from the latter spectroscopic method to interpret the observed Raman spectral features. In the confocal optical mode adopted in this study (with the laser collimated on the sample surface), the Raman probe had an in-depth penetration of about 5 μm, which is not comparable with the 2–5 nm of the XPS probe [86], Nevertheless, exploiting the confocality of the Raman probe, we could observe additional interesting features for the N_2-thermal treated and polished surfaces. The doubled triplet in Fig. 4(b) should be assigned to a form of β-Si(Y)AlON, as also suggested by XPS analyses. For this material, XPS analyses revealed N/Si and O/Si atomic ratios which correspond to silicon oxynitride, Si_2N_2O, and also the highest amount of Al and Y among the set of examined samples. However, as previously mentioned, these ratios are strictly valid only for the first few nanometers of the sample thickness, while the Raman probe averages the signal over about three orders of magnitude larger depth. The line map taken along the z-axis of the
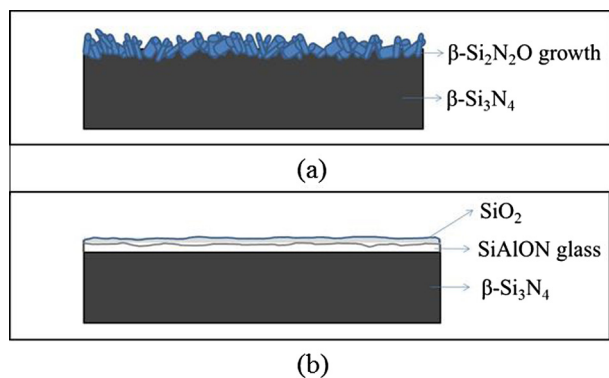
Fig. 7. Schematic representation of the thermally treated samples: (a) in N_2 and (b) in air. In (a), the blue crystals represent the non-stoichiometric β-Sialon compound grown during the treatment in N_2. In (b), the white layers represent SiO_2 and SiAlON glasses.

sample polished and then thermally-treated in N_2 (*cf.* Fig. 5) shows the doubled triplet disappearing as the focus is taken deeper into the sample, suggesting that the above-mentioned β-Si(Y)AlON compound is uniformly present down to a depth on the order of the tens of micron below the free surface. As seen in the micrographs (*cf.* Fig. 1(b, e) and Fig. 6(b, c)), the thermally-treated samples show a different texture as compared to the untreated specimens, which is especially marked after the N_2 thermal treatments. According to Raman and microscopy findings, annealing in N_2 environment promoted the re-growth of a surface layer of off-stoichiometric β-Si(Y)AlON, a newly formed compound responsible for the observed (shifted and broadened) Raman triplet. Note that this process does not seem to equally take place for the sample annealed in air, in which only an external glassy layer formed with a composition including, according to XPS, smaller amounts of Al and Y, and with a Raman spectrum close to that of silica glass. The modifications induced by the thermal treatments are schematically depicted in Fig. 7(a) and (b) for N_2 and air annealed samples, respectively. Finally, a systematic study by Takase and Tani might allow us to relate both shift and broadening of the Raman bands (*i.e.*, as observed at the surface of the N_2-treated sample) to the lattice constants and, thus, to the stoichiometry of the hexagonal cell [88]. The observed frequency shifts are mainly a result of changes in force constants, which are related to variations in interatomic distances and bonding. In SiAlON compounds ($Si_{6-z}Al_zO_zN_{8-z}$), silicon and nitrogen of the β-Si_3N_4 network are partly substituted by aluminum and oxygen, respectively [89]. As z increases, elemental substitutions result in an incremental degree of structural disorder in the β-Si_3N_4 network, giving rise to a decrease in force constant of the Si–N bond. In other words, as z increases, a shift of the Raman bands toward lower frequencies can be observed together with their broadening. A shift of ~ 4 cm^{-1} toward lower frequencies of the Si–N skeletal vibration at ~ 180 cm^{-1} corresponds to a variation in lattice constant Δa of ~ 0.001 nm, which in turn corresponds to a dilute stoichiometry in the order of $z \sim 0.3$.

5. Conclusions

It was found that the surface chemistry and morphology of a Si_3N_4 bioceramic could be varied significantly through conventional thermal, chemical, and mechanical treatments. The surface of as-fabricated Si_3N_4 exhibited anisotropic and stochastically oriented β-Si_3N_4 grains covered with a thin Si_2N_2O-like passivation layer, strong negative charging at biologic pH, and moderate hydrophilicity that improved over time as capillary forces drew

water into the spaces between the surface grains. Etching in HF or subjecting the material to CMP produced a surface composition with a higher N/Si and lower O/Si ratios than as-fabricated materials – which exhibited strong negative surface charging at homeostatic pH and moderate hydrophilicity. Thermal treatment in N_2 produced a surface coated in crystalline β-Si(Y)AlON precipitates whose concentration decreased as a function of depth up to ~ 90 μm. This treatment condition exhibited extreme hydrophilicity. Thermal treatment in an oxidizing atmosphere resulted in a surface composition effectively the same as amorphous SiO_2. It also exhibited extremely low wetting angles and charging behavior that mimicked pure silica. The isoelectric points of these variously treated samples increased with decreasing O/Si and with increasing N/Si atomic ratio, as the surfaces transitioned from resembling pure SiO_2 to pure Si_3N_4, correlating well with observations made in the previously cited studies. Both the thermal treatments (*i.e.*, oxidation and under N_2) may offer interesting advantages for orthopaedic implants due to their observed extreme hydrophilicity. The large negative surface charge at homeostatic pH observed for the as-fabricated Si_3N_4 may contribute to its bacteriostatic and osteointegrative behavior. The significant increase in the surface charge for the oxidized material may lead to an enhancement of these properties over what has already been observed for the as-fabricated material. Further, the surface chemistry of silica is well-understood, lends itself to manipulation, and has already been shown to be an ideal scaffold for bone on-growth. A material that exhibits the flexibility of silica's surface chemistry mated with the desirable bulk mechanical properties of dense Si_3N_4 could be readily engineered and adapted to several implant applications. Consequently, future studies will be focused in three areas: (1) Varying the parameters of the thermal treatments and observing corresponding surface chemistry; (2) *In vitro* tests examining the treated surface's interaction with relevant proteins, human cells (such as mesenchymal stem cells and osteoblasts), and nosocomial bacteria; and (3) *In vivo* examination of the performance of modified surfaces in complex, living systems.

6. Disclosures

Acknowledgements

References

[1] M.N. Rahaman, A. Yao, B.S. Bal, J.P. Garino, M.D. Ries, Ceramics for prosthetic hip and knee joint replacement, J. Am. Ceram. Soc. 90 (2007) 1965–1988.

[2] M. Mazzocchi, A. Bellosi, On the possibility of silicon nitride as a ceramic for structural orthopaedic implants. Part I: processing, microstructure, mechanical properties, cytotoxicity, J. Mater. Sci. – Mater. Med. 19 (2008) 2881–2887.

[3] M. Mazzocchi, D. Gardini, P.L. Traverso, M.G. Faga, A. Bellosi, On the possibility of silicon nitride as a ceramic for structural orthopaedic implants. Part II: chemical stability and wear resistance in body environment, J. Mater. Sci. – Mater. Med. 19 (2008) 2889–2901.

[4] B.S. Bal, M.N. Rahaman, Orthopedic applications of silicon nitride ceramics, Acta Biomater. 8 (2012) 2889–2898.

[5] R.M. Taylor, J.P. Bernero, A.A. Patel, D.S. Brodke, A.C. Khandkar, Silicon nitride – a new material for spinal implants, J. Bone Joint Surg. Br. 92 (2010) 133.

[6] F.F. Lange, Relation between strength, fracture energy, and microstructure of hot-pressed Si_3N_4, J. Am. Ceram. Soc. 56 (1973) 518–522.

[7] F.L. Riley, Silicon nitride and related materials, J. Am. Ceram. Soc. 83 (2000) 245–265.

[8] F.F. Lange, The sophistication of ceramic science through silicon nitride studies, J. Ceram. Soc. Jpn. 114 (2006) 873–879.

[9] P.F. Becher, E.Y. Sun, K.P. Plucknett, K.B. Alexander, C. Hsueh, H. Lin, et al., Microstructural design of silicon nitride with improved fracture toughness : I. Effects of grain shape and size, J. Am. Ceram. Soc. 81 (1998) 2821–2830.

[10] K. Bodišová, M. Kašiarová, M. Domanická, M. Hnatko, Z. Lenčéš, Z.V. Nováková, et al., Porous silicon nitride ceramics designed for bone substitute applications, Ceram. Int. 39 (2013) 8355–8362.

[11] M.P. Arts, J.F.C. Wolfs, T.P. Corbin, The CASCADE trial: effectiveness of ceramic versus PEEK cages for anterior cervical discectomy with interbody fusion; protocol of a blinded randomized controlled trial, BMC Musculoskelet. Disord. 14 (2013) 244.

[12] R.F. Kersten, S.M. van Gaalen, M.P. Arts, K.C.B. Roes, A. de Gast, T.P. Corbin, et al., The SNAP trial: A double blind multi-center randomized controlled trial of a silicon nitride versus a PEEK cage in transforaminal lumbar interbody fusion in patients with symptomatic degenerative lumbar disc disorders: study protocol, BMC Musculoskelet. Disord. 15 (2014) 57.

[13] R. Kue, A. Sohrabi, D. Nagle, C. Frondoza, D. Hungerford, Enhanced proliferation and osteocalcin production by human osteoblast-like MG63 cells on silicon nitride ceramic discs, Biomaterials 20 (1999) 1195–1201.

[14] C.R. Howlett, E. McCartney, W. Ching, The effect of silicon nitride ceramic on rabbit skeletal cells and tissue, Clin. Orthop. Relat. Res. 244 (1989) 293–304.

[15] A. Neumann, T. Reske, M. Held, K. Jahnke, C. Ragoss, H.R. Maier, Comparative investigation of the biocompatibility of various silicon nitride ceramic qualities in vitro, J. Mater. Sci. – Mater. Med. 15 (2004) 1135–1140.

[16] C. Santos, S. Ribeiro, J.K.M.F. Daguano, S.O. Rogero, K. Strecker, C.R.M. Silva, Development and cytotoxicity evaluation of SiAlONs ceramics, Mater. Sci. Eng. C27 (2007) 148–153.

[17] C.C. Sorrell, P.H. Hardcastle, R.K. Druitt, C.R. Howlett, E.R. McCartney, Results of 15-year clinical study of reaction bonded silicon nitride intervertebral spacers, in: Proc. 7th World Biomater. Conf. (2004) 1872.

[18] A. Neumann, M. Kramps, C. Ragoß, H.R. Maier, K. Jahnke, Histological and microradiographic appearances of silicon nitride and aluminum oxide in a rabbit femur implantation model, Materwiss Werksttech 35 (2004) 569–573.

[19] C.C. Guedes-e-Silva, B. Konig, M.J. Carbonari, M. Yoshimoto, S. Allegrini, J.C. Bressiani, Tissue response around silicon nitride implants in rabbits, J. Biomed. Mater. Res. 84A (2008) 337–343.

[20] M. Anderson, J. Bernero, D. Brodke, Medical imaging characteristics of silicon nitride ceramic a new material for spinal arthroplasty implants, in: 8th Annu. Spine Arthroplast. Soc. Glob. Symp. Motion Preserv. Technol., Miami, FL (2008) 547.

[21] M.C. Anderson, R. Olsen, Bone ingrowth into porous silicon nitride, J. Biomed. Mater. Res. – Part A 92 (2010) 1598–1605.

[22] D.J. Gorth, S. Puckett, B. Ercan, T.J. Webster, M. Rahaman, B.S. Bal, Decreased bacteria activity on Si_3N_4 surfaces compared with PEEK or titanium, Int. J. Nanomed. 7 (2012) 4829–4840.

[23] T.J. Webster, A.A. Patel, M.N. Rahaman, B.S. Bal, Anti-infective and osteointegration properties of silicon nitride, poly (ether ether ketone), and titanium implants, Acta Biomater. 8 (2012) 4447–4454.

[24] Personal Communication from William Jordan, Director of Regulatory Affairs and Quality Assurance, Amedica Corporation, Salt Lake City, UT 84119 (2014).

[25] B.S. Bal, A. Khandkar, R. Lakshminarayanan, I. Clarke, A.A. Hofmann, M.N. Rahaman, Testing of silicon nitride ceramic bearings for total hip arthroplasty, J. Biomed. Mater. Res. Part B Appl. Biomater. 87 (2008) 447–454.

[26] B.S. Bal, A. Khandkar, R. Lakshminarayanan, I. Clarke, A.A. Hofmann, M.N. Rahaman, Fabrication and testing of silicon nitride bearings in total hip arthroplasty, J. Arthroplasty 24 (2009) 110–116.

[27] M. Rahaman, Y. Boiteux, L. DeJonghe, Surface characterization of silicon nitride and silicon carbide powders, Bull. Am. Ceram. Soc. 65 (1986) 1171–1176.

[28] NIST-JANAF Thermochemical Tables, <http://kinetics.nist.gov/janaf/> (2015).

[29] S.I. Raider, R. Flitsch, J.A. Aboaf, W.A. Pliskin, Surface oxidation of silicon nitride films, J. Electrochem. Soc. 123 (1976) 560–565.

[30] L. Bergström, R.J. Pugh, Interfacial characterization of silicon nitride powders, J. Am. Ceram. Soc. 72 (1989) 103–109.

[31] V.A. Hackley, P. Sen Wang, S.G. Malghan, Effects of soxhlet extraction nitride powders on the surface oxide layer of silicon nitride powders, Mater. Chem. Phys. 36 (1993) 112–118.

[32] D.P. Butt, D. Albert, T.N. Taylor, Kinetics of thermal oxidation of silicon nitride powders, J. Am. Ceram. Soc. 79 (1996) 2809–2814.

[33] J. Szépvölgyi, I. Mohai, J. Gubicza, Studies on atmospheric ageing of nanosized silicon nitride powders, Key Eng. Mater. 264–268 (2004) 2311–2314.

[34] G. Busca, V. Lorenzelli, G. Porcile, M.I. Baraton, P. Quintard, R. Marchand, FT-IR study of the surface properties of silicon nitride, Mater. Chem. Phys. 14 (1986) 123–140.

[35] S. Mezzasalma, Characterization of silicon nitride surface in water and acid environment: a general approach to the colloidal suspensions, J. Colloid Interface Sci. 180 (1996) 413–420.

[36] R.K. Iler, The Chemistry of Silica, Wiley, New York, NY, 1979.

[37] P. Greil, R. Nitzsche, H. Friedrich, W. Hermel, Evaluation of oxygen content on silicon nitride powder surface from the measurement of the isoelectric point, J. Eur. Ceram. Soc. 7 (1991) 353–359.

[38] J. Sonnefeld, Determination of surface charge density parameters of silicon nitride, Colloids Surf. A 108 (1996) 27–31.

[39] J.S. Reed, Principles of Ceramics Processing, second ed., Wiley, New York, 1995.

[40] J.N. Israelachvili, Intermolecular and Surface Forces, third ed., Academic Press, London, 2011.

[41] A.V. Delgado, F. González-Caballero, R.J. Hunter, L.K. Koopal, J. Lyklema, Measurement and interpretation of electrokinetic phenomena, J. Colloid Interface Sci. 309 (2007) 194–224.

[42] P. Greil, Processing of silicon nitride ceramics, Mater. Sci. Eng. A 109 (1989) 27–35.

[43] J.A. Lewis, Colloidal processing of ceramics, J. Am. Ceram. Soc. 83 (2000) 2341–2359.

[44] D. Jan, S. Raghavan, Electrokinetic characteristics of nitride wafers in aqueous solutions and their impact on particulate deposition, J. Electrochem. Soc. 141 (1994) 2465–2469.

[45] J. Homeny, L.J. Neergaard, K.R. Karasek, J.T. Donner, S.A. Bradley, Characterization of ß-silicon nitride whiskers, J. Am. Ceram. Soc. 73 (1990) 102–105.

[46] M. Tokuse, R. Oyama, H. Nakagawa, I. Nakabayashi, Characterization of the oxidized β-Si_3N_4 whisker surface layer using XPS and TOF-SIMS, Anal. Sci. 17 (2001) 281–284.

[47] I. Iturriza, F. Castro, M. Fuentes, Sinter and sinter-HIP of silicon nitride ceramics with yttria and alumina additions, J. Mater. Sci. 24 (1989) 2047–2056.

[48] G.A. Parks, The isoelectric points of solid oxides, solid hydroxides, and aqueous hydroxo complex systems, Chem. Rev. 65 (1965) 177–198.

[49] G.V. Franks, Y. Gan, Charging behavior at the alumina-water interface and implications for ceramic processing, J. Am. Ceram. Soc. 90 (2007) 3373–3388.

[50] K.J. Trevino, J.C. Shearer, P.R. McCurdy, S.E. Pease-Dodson, C.C. Okegbe, E.R. Fisher, Isoelectric points of plasma-modified and aged silicon oxynitride surfaces measured using contact angle titrations, Surf. Interface Anal. 43 (2011) 1257–1270.

[51] A. Schroeder, E. van der Zypen, H. Stich, F. Sutter, The reactions of bone, connective tissue, and epithelium to endosteal implants with titanium-sprayed surfaces, J. Maxillofac. Surg. 9 (1981) 15–25.

[52] B. Kasemo, J. Lausmaa, Biomaterial and implant surfaces: a surface science approach, Int. J. Oral Maxillofac. Implants 3 (1988) 247–259.

[53] S.G. Steinemann, Metal implants and surface reactions, Injury 27 (1996). S/C16–S/C22.

[54] B.D. Boyan, T.W. Hummert, D.D. Dean, Z. Schwartz, Role of material surfaces in regulating bone and cartilage cell response 17 (1996) 137–146.

[55] T. Masuda, G.E. Salvi, S. Offenbacher, D.A. Felton, L.F. Cooper, Cell and matrix reactions at titanium implants in surgically prepared rat tibiae, Int. J. Oral Maxillofac. Implant 12 (1996) 472–485.

[56] L.L. Hench, J.M. Polak, Third-generation biomedical materials, Science 295 (2002) 1014–1017.

[57] Q.Z. Chen, I.D. Thompson, A.R. Boccaccini, 45S5 bioglass-derived glass-ceramic scaffolds for bone tissue engineering, Biomaterials 27 (2006) 2414–2425.

[58] T. Kokubo, Apatite formation on surfaces of ceramics, metals and polymers in body environment, Acta Mater. 46 (1998) 2519–2527.

[59] T. Kokubo, H. Takadama, How useful is SBF in predicting in vivo bone bioactivity?, Biomaterials 27 (2006) 2907–2915

[60] M. Hermansson, The DLVO theory in microbial adhesion, Colloids Surf. B 14 (1999) 105–119.

[61] M. Katsikogianni, Y.F. Missirlis, Concise review of mechanisms of bacterial adhesion to biomaterials and of techniques used in estimating bacteria-material interactions, Eur. Cells Mater. 8 (2004) 37–57.

[62] B. Derjaguin, L. Landau, Theory of the stability of strongly charged lyophobic sols and of the adhesion of strongly charged particles in solutions of electrolytes, Acta Phys. Chem. URSS (1941) 14.

[63] E.J.W. Verwey, J.T.G. Overbeek, Theory of the Stability of Lyophobic Colloids, Elsevier Publishing Company Inc., 1948.

[64] G. Roebben, C. Sarbu, T. Lube, O. Van der Biest, Quantitative determination of the volume fraction of intergranular amorphous phase in sintered silicon nitride, Mater. Sci. Eng. A 370 (2004) 453–458.

[65] A. Witvrouw, B. Du Bois, P. De Moor, A. Verbist, C.A. Van Hoof, H. Bender, Comparison Between wet HF etching and vapor HF etching for sacrificial oxide

removal, in: Micromach. Microfabr., International Society for Optics and Photonics, 2000, pp. 130–141.

[66] J. Bühler, F.P. Steiner, H. Baltes, Silicon dioxide sacrificial layer etching in surface micromachining, J. Micromech. Microeng. 7 (1997) R1.

[67] K.R. Williams, K. Gupta, M. Wasilik, Etch rates for micromachining processing-part II, J. Microelectromech. Syst. 12 (2003) 761–778.

[68] A. Marmur, Wetting on hydrophobic rough surfaces: to be heterogeneous or not to be?, Langmuir 19 (2003) 8343–8348

[69] L.-C. Xu, C.A. Siedlecki, Submicron-textured biomaterial surface reduces staphylococcal bacterial adhesion and biofilm formation, Acta Biomater. 8 (2012) 72–81.

[70] X-Ray Photoelectron MicroscopyAm. Soc. Met. Int. ASM Handbook vol. 10 Mater. Charact., ASM Int., USA, 1986, pp. 568–580. 65.

[71] D.R. Clarke, F.F. Lange, Oxidation of Si_3N_4 alloys: relation to phase equilibria in the system Si_3N_4-SiO_2-MgO, J. Am. Ceram. Soc. 63 (1980) 586–593.

[72] D.R. Clarke, F.F. Lange, G.D. Schnittgrund, Strengthening of a sintered silicon nitride by a post-fabrication heat treatment, J. Am. Ceram. Soc. 65 (1982) C51–C52.

[73] L. Wang, C. He, J. Wu, Oxidation of sintered silicon nitride: I. Phase composition and microstructure, Mater. Sci. Eng. A 157 (1992) 125–130.

[74] V.P. Hairden, J. Harris, The isoelectric point of bacterial cells, J. Bacteriol. 65 (1953) 198–202.

[75] M. Horka, P. Karasek, F. Ruzicka, M. Dvorackova, M. Sittova, M. Roth, Separation of methicillin-resistant from methicillin-susceptible *Staphylococcus aureus* by electrophoretic methods in fused silica capillaries etched with supercritical water, Anal. Chem. 86 (2014) 9701–9708.

[76] B.A. Jucker, H. Harms, A.J.B. Zehnder, Adhesion of the positively charged bacterium *Stenotrophomonas* (*Xanthomonas*) *maltophilia* 70401 to glass and teflon, J. Bacteriol. 178 (1996) 5472–5479.

[77] A. Arafat, K. Schroën, L.C.P.M. De Smet, E.J.R. Sudhölter, H. Zuilhof, Tailor-made functionalization of silicon nitride surfaces, J. Am. Chem. Soc. 126 (2004) 8600–8601.

[78] J. Bico, U. Thiele, D. Quéré, Wetting of textured surfaces, Colloids Surf. A 206 (2002) 41–46.

[79] R.R. Thomas, F.B. Kaufman, J.T. Kirleis, R.A. Belsky, Wettability of polished silicon oxide surfaces, J. Electrochem. Soc. 143 (1996) 643–648.

[80] J. Diao, D. Ren, J.R. Engstrom, K.H. Lee, A surface modification strategy on silicon nitride for developing biosensors, Anal. Biochem. 343 (2005) 322–328.

[81] K. Honda, S. Yokoyama, S. Tanaka, Assignment of the Raman active vibration modes of ß-Si3N4 using micro-Raman Scattering, J. Appl. Phys. 85 (1999) 7380–7384.

[82] Y. Sato, S. Motoi, Studies of the state of iron contained in α- and β-silicon nitride by Mössbauer and Raman Effects, J. Phys. Chem. Solids 40 (1979) 1–7.

[83] J. Ballato, P. Dragic, Materials development for next generation optical fiber, Materials (Basel) 7 (2014) 4411–4430.

[84] V. Sergo, G. Pezzotti, G. Katagiri, N. Muraki, T. Nishida, Stress dependence of the Raman spectrum of β-silicon nitride, J. Am. Ceram. Soc. 79 (1996) 781–784.

[85] S. Tochino, G. Pezzotti, Micromechanical analysis of silicon nitride: a comparative study by fracture mechanics and Raman microprobe spectroscopy, J. Raman Spectrosc. 33 (2002) 709–714.

[86] S. Ohtsuka, W. Zhu, S. Tochino, Y. Sekiguchi, G. Pezzotti, In-depth analysis of residual stress in an alumina coating on silicon nitride substrate using confocal Raman piezo-spectroscopy, Acta Mater. 55 (2007) 1129–1135.

[87] I. Tanaka, S. Nasu, H. Adachi, Y. Miyamoto, K. Niihara, Electronic structure behind the mechanical properties of β-Sialons, Acta Metall. Mater. 40 (1992) 1995–2001.

[88] A. Takase, E. Tani, Raman spectroscopic study of β-Sialons in the system Si_3N_4-Al_2O_3-AlN, J. Mater. Sci. Lett. 3 (1984) 1058–1060.

[89] W. Zhu, B. McEntire, Y. Enomoto, M. Boffelli, G. Pezzotti, Point-defect populations as induced by cation/anion substitution in β-Si_3N_4 lattice. A cathodoluminescence study, J. Phys. Chem. C 119 (2015) 3279–3287.